Spectrochimica Acta Part B: Atomic Spectroscopy 180 (2021) 106145

Contents lists available at ScienceDirect

Spectrochimica Acta Part B: Atomic Spectroscopy

journal homepage: www.elsevier.com/locate/sab

Characterization of femtosecond laser ablation processes on as-deposited SnAg solder alloy using laser ablation ionization mass spectrometry

A. Cedeño López [a], V. Grimaudo [b,*], A. Riedo [b], M. Tulej [b], R. Wiesendanger [b], R. Lukmanov [b], P. Moreno-García [a], E. Lörtscher [c], P. Wurz [b], P. Broekmann [a]

[a] Department of Chemistry and Biochemistry, Interfacial Electrochemistry Group, University of Bern, Freiestrasse 3, CH-3012 Bern, Switzerland
[b] Physics Institute, Space Research and Planetary Sciences, University of Bern, Sidlerstrasse 5, CH-3012 Bern, Switzerland
[c] IBM Research - Zurich, Science and Technology Department, Säumerstrasse 4, CH-8803 Rüschlikon, Switzerland

ARTICLE INFO

Keywords:
Laser ablation
Wavelength dependence
Melting point
Surface roughness
Solder bump

ABSTRACT

Laser ablation ionization mass spectrometry studies on polished surface structures of hard, high melting point multicomponent interconnect structures using our femtosecond-laser time-of-flight mass spectrometer have previously been proven capable of providing spatially resolved chemical depth profile data at the micro- and nanometer level. Transfer of experimental protocols tailored to suit such type of samples to low melting point materials with high surface roughness, however, is highly challenging, as thermal effects caused by interactions of the laser light with the targeted surface play a severe role in the latter case and may significantly deteriorate the analysis outcome. In this contribution we present a dedicated and detailed comparison of the distinct effects of near infrared and ultraviolet irradiation on the ablation process in femtosecond laser ablation ionization mass spectrometry studies on low melting point materials. As model substrate we use high surface roughness, as-deposited SnAg solder alloy, a material of major industrial relevance in microchip fabrication. We will demonstrate herein that polydimethylsiloxane replica casting is possible also from granularly structured, high surface roughness samples. Characterization of the laser ablation craters as well as of their polydimethylsiloxane replicas is carried out by mass spectrometric analysis, Scanning Electron Microscopy imaging, and furthermore, as a novel approach for this purpose, by white light interferometry. Integration of all obtained results significantly adds to the detailed understanding of laser ablation processes on low melting point, high surface roughness materials and allows identifying optimal depth profiling conditions for these demanding samples.

1. Introduction

Since the ban of leaded solder materials in response to the 'Directive on Waste from Electrical and Electronic Equipment' that was enforced by 1st January 2004 in Europe, which also affected Asian (especially the Japanese) and US markets, there has been a constant strive to identify suitable substitute materials for the broadly and well established eutectic 63Sn-37Pb and near-eutectic 60Sn-40Pb solders [1].

Among the top candidates, it is the eutectic Sn-3.5Ag alloy with a melting temperature of 221 °C, which has nowadays become the industry standard Pb-free solder for advanced packaging applications (solder bumping) on the 300 mm wafer level [2–7].

The efficient and void-free electrodeposition of SnAg alloy requires the use of several organic plating additives, which may leave a residue embedded in the alloy matrix. Therefore, spatially resolved chemical analysis of the solder structures is highly desirable for quality control and further process development.

Various analytical techniques exist nowadays that can be applied for the quality control of solid materials relevant in the semiconductor industry. There are techniques for surface analysis, which are excellent for probing nanostructured materials (i.e., multilayers and nanocomposites), e.g. X-ray Photoelectron Spectroscopy (XPS) [8], Auger Electron Spectroscopy (AES) [9], (Nano)-Secondary Ion Mass Spectrometry (Nano-SIMS) [8,10], and Glow Discharge Optical Emission Spectroscopy (GDOES) [8,11]. In addition, there are methods probing the bulk composition like Laser Ablation Inductively Coupled Plasma Mass Spectrometry (LA-ICP-MS) [11,12] and Laser-Induced Breakdown Spectroscopy (LIBS) [11,13] exhibiting very good quantitative depth profiling analysis of larger structures.

Laser Ablation Ionization Mass Spectrometry (LIMS) is an analytical

* Corresponding author.
E-mail address: valentine.riedo@space.unibe.ch (V. Grimaudo).

https://doi.org/10.1016/j.sab.2021.106145
Received 8 August 2020; Received in revised form 16 February 2021; Accepted 17 February 2021
Available online 24 February 2021

technique that has recently been proven a suitable approach to deliver spatially resolved chemical data with lateral and vertical resolution at the micro- and nanometer level, respectively [14–17]. However, the inherent physical properties of the SnAg alloy, particularly its softness and low melting temperature, render the analysis by means of laser ablation very demanding and significant side effects that interfere with the desired information may appear depending on the experimental conditions [14].

In the context of laser ablation-inductively coupled plasma-mass spectrometry (LA-ICP-MS), significant differences between laser ablation processes induced by ultraviolet (UV) and infrared (IR) ns-laser irradiation have been reported [18–20]. Largely, this is because IR laser irradiation is less efficiently absorbed by Sn and Ag than UV laser irradiation [21], which results in more pronounced melting and recrystallization phenomena in the former case [19,20]. Concerning the pulse duration, it has been found that fs-UV laser ablation causes much less melting effects than ns-UV laser ablation [22]. Most reports on these aspects, however, have been restricted to nearly ideally flat and hard, high-melting materials at elevated laser pulse energies.

In this contribution, we aim to investigate whether comparable observations hold true in near IR (NIR) and UV fs laser ablation ionization mass spectrometry analysis of rough, soft and low-melting point SnAg solder materials using our LIMS system [23–25]. To the best of our knowledge, only few detailed studies on the fs laser ablation characteristics on a given material for different laser wavelengths under similar experimental conditions on the same basis setup exist [26]. Little has so far been reported on fs-LIMS-based investigations on low melting point, high surface roughness samples representing the real situation of as-deposited solder contact arrays. Our goal in this study is to determine and explain in detail the optimal laser ablation conditions for fs-LIMS that allowed for spatially resolved chemical depth profiling of SnAg solder materials to allow for accurate and quantitative three-dimensional mapping of their chemical composition [27]. For this purpose, we utilize fs-NIR and fs-UV LIMS to generate laser ablation craters and we obtain mass spectrometric data for each laser shot in the process. Furthermore, we characterize the ablation craters directly by means of Scanning Electron Microscopy (SEM) and by white light interferometry (which is a new approach for this purpose) to obtain complementary information on the ablation process. In addition, to overcome aspect ratio-related limitations of interferometric analysis directly on the crater itself, we cast polydimethylsiloxane (PDMS) replicas of the LIMS craters and investigate them by SEM, which has already been proven an excellent methodology for the depth determination of high-aspect ratio craters [28], and by white light interferometry. A schematic summary of the workflow is given in Fig. 1. Note that the crater shape is simplified in this depiction.

2. Experimental section

2.1. Electrochemical deposition (ECD) of Sn/Ag film

Electrodeposited Sn/Ag alloy films were prepared galvanostatically on blanket Si wafer coupons comprising a 100 nm Cu seed layer (Hionix, USA) using a potentiostat/galvanostat PGSTAT128N (Metrohm Autolab, Switzerland). The electrodeposition was carried out under forced convective conditions. For that, the wafer coupons were mounted onto a Cu rotating disk electrode (RDE) and used as the cathode while a Pt wire served as the anode. An Ag/AgCl (3 M KCl) double junction reference electrode (Metrohm, Switzerland) was used. The composition of the plating bath (BASF SE, Ludwigshafen, Germany) and the applied plating parameters are given in Tables 1 and 2, respectively. Note that two different film samples are referred to in the following. Film 1 was plated in presence of a grain refining agent and has a nominal thickness of 2.5 ± 0.7 µm while film 2 was plated without grain refining agent and has a nominal layer thickness of 10 ± 2 µm. This explains the differences in surface morphology seen in Fig. 2 panels a) and c) (film 1) versus b) and d) (film 2).

2.2. LIMS measurements

The basic operation mode and the performance of the LIMS instrument used in this study have been described in detail in previous publications and only a brief description is given in the following [23,24,29]. The experimental setup consists of a miniature time-of-flight mass analyzer (160 mm × ø 60 mm) coupled to a Ti-Sapphire laser system (CPA system, Clark-MXR Inc., USA) to induce ablation and ionization of the sample material. The laser system produces a fundamental beam of 775 nm wavelength with Gaussian beam profile pulses with a temporal width of ~190 fs. Combined with harmonic generators

Table 1
Composition of SnAg plating bath for SnAg bumps.

chemical name	mL
methane sulfonic acid (70%)	25
tin methane sulfonate, stabilized (38%)	6.45
complexed silver methane sulfonate solution (Ag^+: complexing agent = 1:2n)	1.25
surfactant	0.23
grain refiner	0.23 / 0

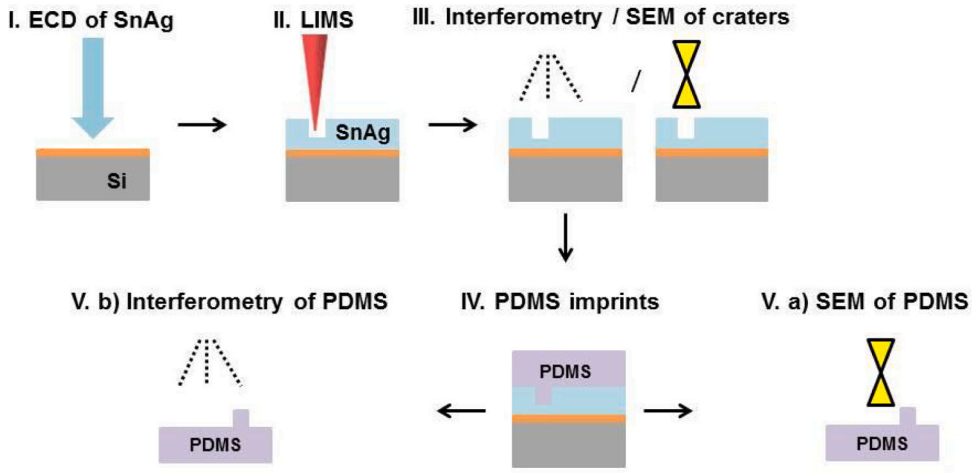

Fig. 1. Schematic summary of the workflow underlying this study on the fs laser ablation characteristics of SnAg alloy films for different laser wavelengths. ECD and PDMS stand for electrochemical deposition and polydimethylsiloxane, respectively.

Table 2
Plating parameters.

Nominal layer thickness (μm)	2.5±0.7 / 10±2
Geometric surface area wafer coupon (cm^2)	0.032
Current density (mA/cm^2)	−150
Rotational speed (rpm)	800

(Storc, Clark-MXR Inc., USA) it provides output radiation at the second (387 nm) and third (258 nm) harmonic of the fundamental beam. Single laser pulses applied to the sample result in ablation and ionization of material and trigger the data acquisition cards to record a TOF spectrum. Two 12 bit high-speed digitizer PCIe cards (U5303A, Keysight, USA), each with two channels recording at 1.6 GS/s, are used for the measurements of single laser shots mass spectra at 1 kHz laser pulse repetition rate. The detection of ions generated during the ablation/ionization process is achieved with a microchannel plate detector (MCP) system in chevron configuration [30]. Only positively charged ions are able to pass the ion optical system of the mass analyzer and arrive at the detector system at time sequences proportional to the square root of their mass-to-charge ratio (TOF principle). The intensity of each element isotope is derived from the measured mass peak profile by a direct integration method using an adaptive Simpson quadrature integration of the mass peaks interpolated by a spline function [31]. An optical microscope system equipped with a modified Nikon 10× objective with a numeric aperture of NA = 0.3 and a spatial resolution of approximately 1 μm was used for precise sample positioning [32]. The fs laser ablation characteristics of SnAg were studied for different numbers of laser shots (1–10′000) at different pulse energies (NIR: 0.20–1.48 μJ; UV: 0.01–0.51 μJ).

2.3. Interferometry

Interferometry micrographs were recorded with a Contour GT interferometer (Bruker, USA) in vertical scanning interferometry (VSI) mode at a magnification of 40×. Analysis of the micrographs was performed with the Bruker Vision64 MapTM software and the Gwyddion software tool.

2.4. PDMS casting

To obtain a negative imprint of the ablated craters in the SnAg layer, a thin (~50 nm) coating (octafluorocyclobutane-based) was deposited on the sample to prevent string adhesion between the PDMS and the substrate. The sample was immobilized inside a Teflon-coated aluminum compartment with a circular opening of 2 mm diameter above the sample area of interest. A custom-made mixture of a polydimethylsiloxane (PDMS) derivative (Sylgard 184, Sigma-Aldrich) was added dropwise inside this opening. Visible gas bubbles were removed by carefully stirring the liquid PDMS. To cure the resin, the setup was annealed in a vacuum furnace at 60 °C for 12 h. This procedure allowed remaining gas to diffuse out of the PDMS and resulted in a void-free negative mold of the sample surface, which could be released from the SnAg sample without inelastic deformation thanks to the high elasticity of the PDMS mold [33]. For the SEM inspection of the PDMS imprints a thin Au layer was sputtered onto the mold to obtain a conductive surface.

2.5. SEM measurements

SEM micrographs were recorded with a Hitachi S-3000 N SEM (Hitachi, Japan) applying an accelerating voltage of 25 kV at a working distance of 10 mm and a Zeiss Leo SEM (Zeiss, Germany) applying an accelerating voltage of 20 kV at a working distance of 8.5 mm.

3. Results and discussion

3.1. Laser ablation crater

Fig. 2 shows top-down SEM micrographs obtained from two different SnAg film samples (film 1: panel a) and c), film 2: panel b) and d))

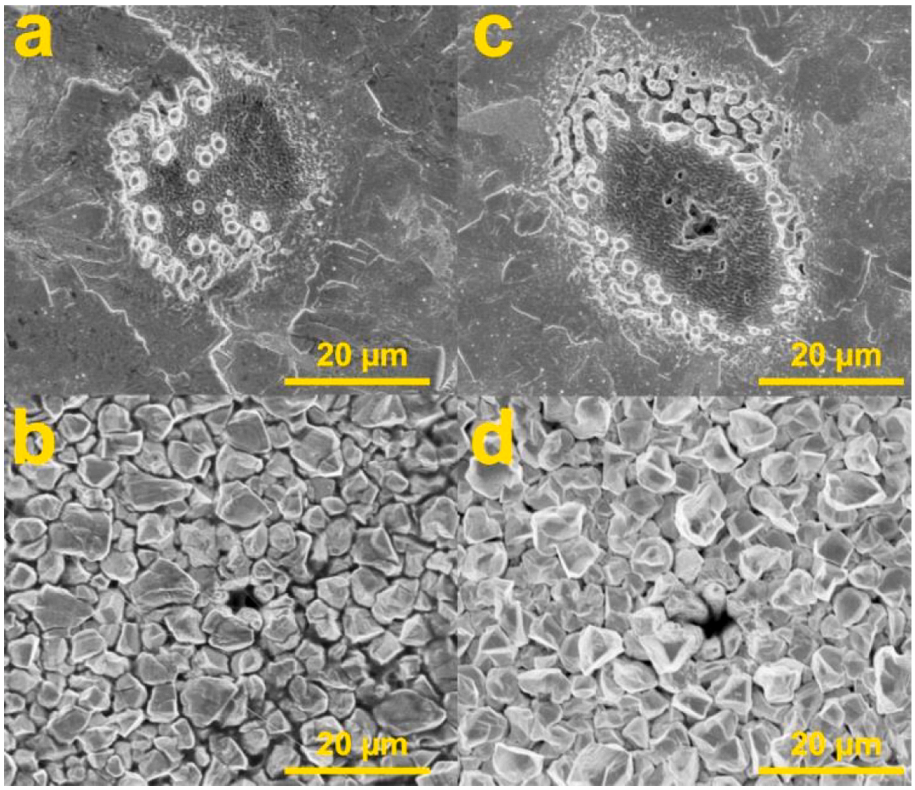

Fig. 2. Top-down SEM micrographs of laser ablation craters resulting from 500 single laser shots with the NIR fs laser (775 nm) and the UV fs laser (258 nm) on two different SnAg film samples (film 1: panels a) and c), film 2: panels b) and d)) at equivalent laser irradiation. Panel a) NIR fs and panel b) UV fs laser crater obtained at 0.7 TW/cm^2. Panel c) NIR fs and panel d) UV fs laser crater obtained at 1.3 TW/cm^2. Note the difference in the size of the affected zones between NIR and UV cases. See Fig. S1 (Appendix) for SEM images of NIR and UV fs craters on film samples with similar surface roughness.

comparing laser ablation craters resulting from 500 single laser shots with a NIR fs laser (775 nm) and a UV fs laser (258 nm) at equivalent irradiance values. Panel a) and b) show the NIR fs and UV fs laser craters, respectively, obtained at a moderate irradiance of 0.7 TW/cm^2. Panel c) and d) present the NIR fs and UV fs laser craters, respectively, obtained at a higher irradiance of 1.3 TW/cm^2. For the NIR fs laser, an actual inner ablation crater can only be distinguished from the affected zone at higher irradiances like the case depicted in panel c). However for both, moderate and elevated irradiances, a large outer affected zone is visible for the NIR fs laser craters as shown in panel a) and c). For most materials, the affected zone is only subject to desorption or slight surface modification phenomena. However, on the low-melting SnAg, as visible in Fig. 2 panel a) and c), severe surface modifications indicative of thermal effects concomitant with evaporation take place in the affected zone [14]. This renders the description of the ablation process based on the mass spectrometric data challenging, as information is sampled not only from the bottom of the actual ablation crater, but with contributions from the affected zone as well. Note that this effect is material specific and not solely a result of the difference in grain size observed in Fig. 2 panels a) and b) compared to panels c) and d). Fig. S1 in the Appendix demonstrates this fact for NIR and UV fs craters on two different SnAg film substrates with a comparable grain size.

3.2. Ablation rate

A common procedure to determine the mean ablation rate is based on the number of single laser shots before observing the onset signal of the underlying substrate material (e.g., Si) in the mass spectra. The principle is depicted in Fig. 3 for the example of the samples studied herein. Panel a) shows an early stage of the ablation process with a shallow crater. Here, the Si signal from the underlying substrate is not detected in the mass spectra. Panel b) shows a crater that just reaches down to the Si substrate. From this point on, isotopically resolved Si is detected in the mass spectra. The onset of Si signal in the mass spectra is considered as the reference for the determination of the mean ablation rate. An example of a depth profile for Si derived from a LIMS measurement at 0.51 μJ is shown in the inset of Fig. 3. The Si signal onset is clearly visible in the depth profile.

In experimental cases like the one depicted in Fig. 2 panel a) and c) in '3.1 Laser ablation crater', the described approach to determine the mean ablation rate based on the onset of the Si signal in the mass spectra must be applied very cautiously. This is because on low melting point samples such as SnAg, melting and evaporation occur preferentially along the grain boundaries, which may result in the formation of pores and channels reaching down to the underlying support material. As a result, the support material may be detected in the mass spectra even though the SnAg layer is not yet completely removed (see Fig. S2 (Appendix)). Besides that, the strongly increased degree of side-walls contributions due to the poor definition of the ablation crater significantly reduces the spatial resolution of the obtained mass spectrometric data [14,17].

It has been reported for LA-ICP-MS that a clear improvement of the ablation process can be achieved by changing the laser wavelength from the NIR to the UV regime [19,20]. However, most of these studies utilized ns lasers, where significantly higher laser pulse energies were applied, and the investigated materials were much harder than the SnAg alloy studied herein [34].

Fig. 2 panel b) shows a crater obtained with our LIMS instrument using an UV fs laser with a wavelength of 258 nm at an irradiance of 0.7 TW/cm^2. In contrast to the NIR fs laser case depicted in Fig. 2 panel a), the crater resulting from the same number of laser shots applied to the SnAg surface with the UV fs laser exhibits a much more defined, significantly smaller ablation crater with hardly any noticeable affected zone and strongly reduced melting and recrystallisation phenomena. Even at these moderate irradiance conditions, we observe that ablation occurs basically unaffected by the SnAg grain boundaries when working with the UV fs laser, which is in strong contrast to the observations made when working with the NIR fs laser as shown in Fig. 2 panel a). Also at elevated irradiances as shown in Fig. 2 panel d) for the UV fs laser and in Fig. 2 panel c) for the NIR fs laser, the pronounced differences in ablation behavior of the two laser setups are evident.

In Fig. 4, the mean ablation rate in [nm/shot] as determined from mass spectrometric data analysis is plotted as a function of the laser irradiance in [TW/cm^2] for both the NIR (black squares) and UV (red circles) fs laser measurements. The data points shown are mean values of three independent repeat experiments with the respective standard deviations. Constant ablation crater diameters of 20 μm for the NIR fs laser and 10 μm for the UV fs laser are assumed, which is based on findings from previous NIR fs laser studies [14,27]. The different ranges shown for the two data sets are due to different available sample layer thicknesses in the separate studies (NIR: 2.5 μm, UV: 10 μm). Clear differences can be seen between the laser ablation characteristics. While the

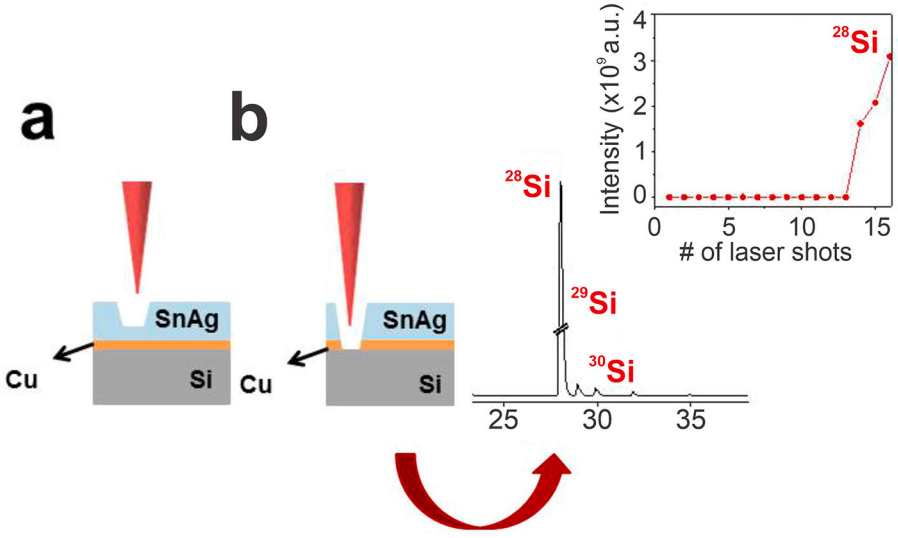

Fig. 3. Approach to determination of the mean ablation rate. Panel a) shows an early state of the ablation with a shallow crater in the SnAg layer. Panel b) shows a crater that has just drilled into the Si wafer. From this point on, isotopically resolved Si signal is detectable in the mass spectra. The inset gives a representative depth profile for ^{28}Si obtained from a LIMS measurement at 0.51 μJ. The ^{28}Si signal onset is clearly visible.

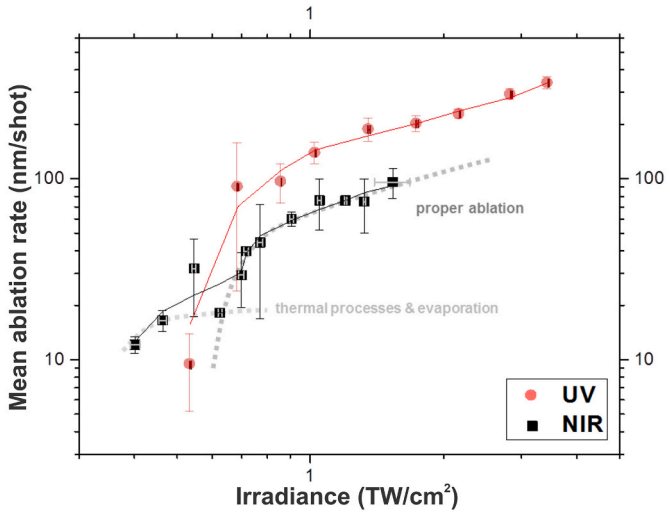

Fig. 4. The mean ablation rate as function of irradiance for the experimentally assessed parameter range. The black squares depict data points obtained for the NIR, the red circles for the UV fs laser system The data points shown are mean values of three independent repeat experiments with the respective standard deviations. The different ranges of the data set are the result of different available layer thicknesses used in the two separate studies (NIR: 2.5 μm, UV: 10 μm). The regimes of dominant melting and evaporation and that of ablation are indicated with independent gray dashed lines. (For interpretation of the references to colour in this figure legend, the reader is referred to the web version of this article.)

NIR fs laser curve displays a rather variable behavior of the ablation rate increase with laser irradiance, the UV fs laser ablation increases more smoothly with laser irradiance and shows increased standard deviations only near the ablation threshold, where the signal-to-noise ratio of the mass spectra impairs data analysis. At slightly elevated laser pulse energies, it reflects an almost perfect linear dependence of the ablation rate on the irradiance. This is most likely because the absorption efficiency of laser light in the UV case is much higher than in the NIR case. As a consequence, the electronic excitation and eventual release of material, which is mainly responsible for the formation of an ablation crater [35], are more pronounced in the UV case. For NIR laser irradiation, less energy per unit volume is absorbed by the electrons in the sample. A fraction of the energy propagates thermally in the material, which is accompanied by melting, evaporation and recrystallization phenomena [19,20,36,37]. These processes compete with instantenous material removal in an irradiance-dependent manner, causing the unsteady shape of the NIR curve and making it hard to define stable working conditions. This also manifests in the larger standard deviations for the NIR than for UV data points. Based on the experimental data for the NIR laser, it can be assumed that, below the ablation threshold, heating of the sample surface at the laser spots results in melting and evaporation of SnAg material. These processes may be considered the dominant sources of signal in this irradiance regime. This concept is indicated by the light gray dashed line with a shallow slope in Fig. 4. After exceeding the ablation threshold, the observed behavior clearly changes as ablation is now the dominant process. This phenomenon is indicated by the dark gray dashed line with a steeper slope in Fig. 4. Depth profiling should only be considered for irradiances above this transition value. Nonetheless, melting and evaporation occur in this parameter regime as well, yet only with reduced relative contribution to the detected signal.

For low-melting point materials like SnAg, the transition between the regime of predominant melting and evaporation and the regime of predominant ablation is observed much more clearly for the NIR fs laser irradiation than for the UV fs laser irradiation. For a more accurate interpretation of the processes occurring on the samples upon laser irradiation it is necessary to perform two- and three-dimensional analysis of the resulting surface morphology and craters. Fig. S3 in the Supplementary Data (Appendix) compares interferometric topographic analyses of laser craters obtained on SnAg film samples with both NIR and UV fs lasers.

All discussed findings clearly point to the superiority of using an UV fs laser rather than a NIR fs laser in depth profiling applications of SnAg solder alloy as one typical example for high surface roughness, low melting point materials, which has not been studied in this detail before. Note that the ablation rate per single UV fs laser shot (vertical spatial resolution in depth profile studies) could be improved when further approaching the ablation threshold. However, for the scope of this application-oriented study, we restricted our following UV fs LIMS investigations to the target parameter range for depth profile analysis of industrially relevant solder bump structures with a surface roughness in the μm range. For the current UV fs laser setup, this parameter range is characterized by a minimum irradiance of around 1 TW/cm^2 and a mean ablation rate of 100–200 nm/shot.

3.3. Crater depth

In a next step, to obtain information on the crater depths of very shallow craters as well and to determine the mean ablation rate by a further and independent approach, white light interferometry was performed on the ablation craters. Fig. 5 panel a) shows a representative interferometry image of the SnAg surface with seven visible UV fs laser craters indicated by the white arrows. Panel b) shows a line scan derived from the crater indicated by the red line in panel a). This crater is just a representative example. Note that for data analysis, only craters ≤10 μm (i.e. derived from the SnAg film) were considered. For typical examples of shallower craters see Fig. S4 in the Supplementary Data (Appendix). Each crater was analysed concerning its depth by a vertical and horizontal line scan to account for non-symmetric features. As can be seen in panel b), the interferometry measurements yielded a detailed representation of the crater shape and depth. For comparison with interferometry of NIR fs laser craters, see Fig. S5 in the Appendix.

3.4. 3D crater analysis

After extracting the required depth information on the unchanged sample, PDMS imprints of the ablation craters were cast to obtain novel insights regarding the ablation characteristics of low melting point, high surface roughness materials like SnAg. After removal from the sample surface, the PDMS imprints were sputter coated with several nm of Au and imaged by SEM. It was found that, despite the high sample surface roughness, the granular structure and the low melting temperature of that alloy, PDMS casting works out very well also on SnAg. Craters of a sufficient depth were both distinguishable from the root mean squared (RMS) surface roughness and reproduced in high detail. Fig. 6 displays representative SEM micrographs of PDMS imprints of craters obtained with the UV fs laser. For a general comparison with the morphology of PDMS imprints obtained from NIR fs laser craters see Fig. S6 in the Supplementary Data (Appendix). Panel a) of Fig. 6 depicts an overview image showing the decrease in the height of the crater negatives with decreasing number of applied laser shots along the diagonal from the upper left to the lower right corner. Panel b) is a zoom-in on one crater negative, that clearly drilled deep into the Si substrate, which becomes obvious due to its height > 20 μm.

After the white light interferometry measurements had provided good results with respect to the 3D structure of the ablation craters, we tested white light interferometry also on the PDMS imprints, i.e. the negatives of the craters. Fig. 7 panel a) shows a representative interferometry measurement of a selected area on the PDMS imprint of the SnAg sample, i.e. the range of 10′000 to 500 (left to right) laser shots conducted at 0.32 μJ. The red and black lines indicate the selected crater and the orientation of the line scans over its surface shown in panel b). This particular crater is deeper than 10 μm, which means it reached

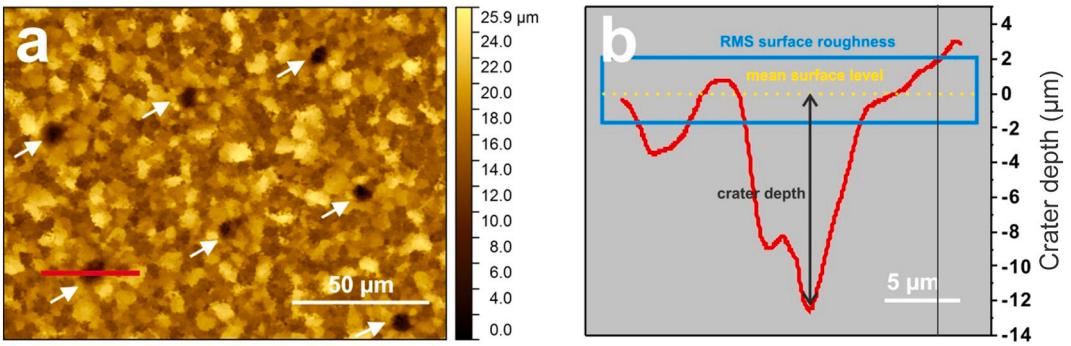

Fig. 5. a) Representative white light interferometry image of the SnAg alloy surface. UV fs laser crater locations are indicated by white arrows, location of line scan by the red bar. b) Example of a line scan used to determine the crater depth, derived from the red line shown in panel a). (For interpretation of the references to colour in this figure legend, the reader is referred to the web version of this article.)

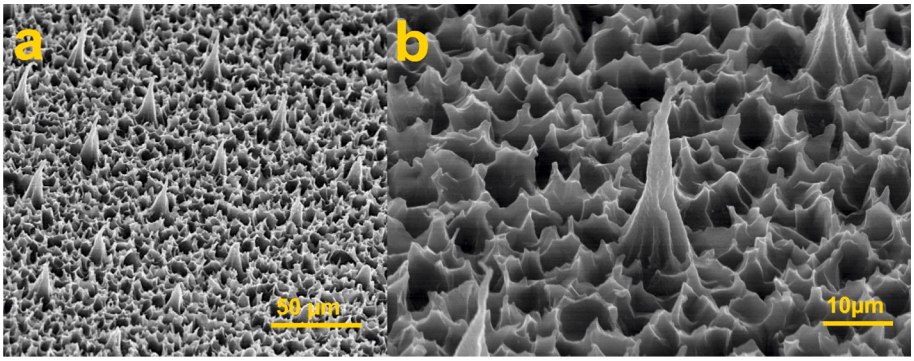

Fig. 6. PDMS imprints of representative UV fs laser craters. Although the sample surface has an intrinsic roughness, craters of a certain depth can clearly be distinguished.

down to the Si substrate. It is shown here due to the ease of distinction from the surrounding surface roughness as a proof of concept for the PDMS molding methodology on high surface roughness samples like the SnAg films shown. It can be seen that interferometric analysis of the PDMS imprints is possible when they are sputtered with a few nm of a non-transparent material, e.g. Au in this particular case.

In Fig. 8, we compare the results for the determination of the mean ablation rate with the UV fs laser by means of mass spectrometric data analysis shown as orange diamonds with those obtained from the white light interferometry measurements shown as green circles. Every interferometry data point is the average of 3 individual repeat craters obtained with 500 single laser shots at different pulse energies analysed by two perpendicular line scans each. The error bar represents the associated standard deviation. Note that only SnAg derived craters ($\leq$ 10 µm) were considered for interferometric data analysis, not such craters that reached into the underlying Si substrate. Every mass spectrometric data point is the average of 5 individual repeat craters obtained with 10′000 single laser shots at different pulse energies with the related standard deviation as error bar. As can be seen in Fig. 8, there is a very good agreement between the mass spectrometric and interferometric determination of the mean ablation rates, which supports suitability of both approaches. The high surface roughness of the

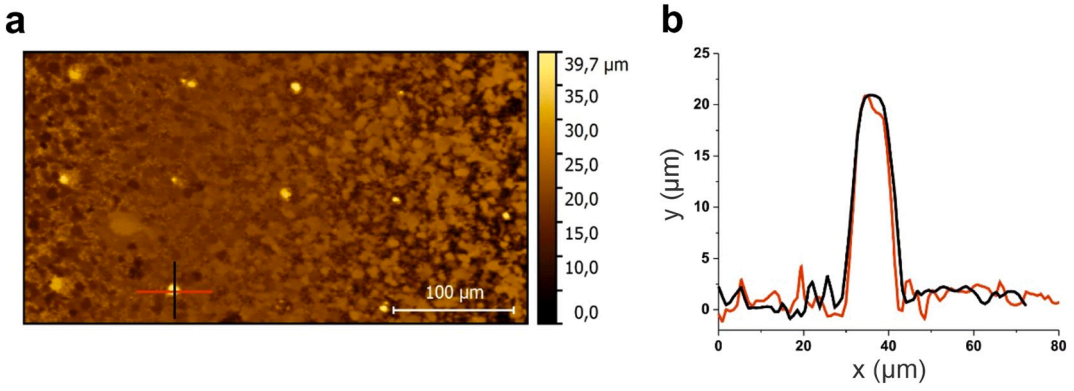

Fig. 7. White light interferometric analysis of the PDMS imprint of a selected area on the SnAg wafer coupon. Panel a) Overview image of UV fs laser pulse counts 10′000 to 500 (left to right) at 0.32 µJ. The red and black line indicate the selected crater and the orientation of the line scans over its surface shown in panel b). Panel b) Line scans in y and x direction over a crater formed by 5′000 laser shots at 0.32 µJ. (For interpretation of the references to colour in this figure legend, the reader is referred to the web version of this article.)

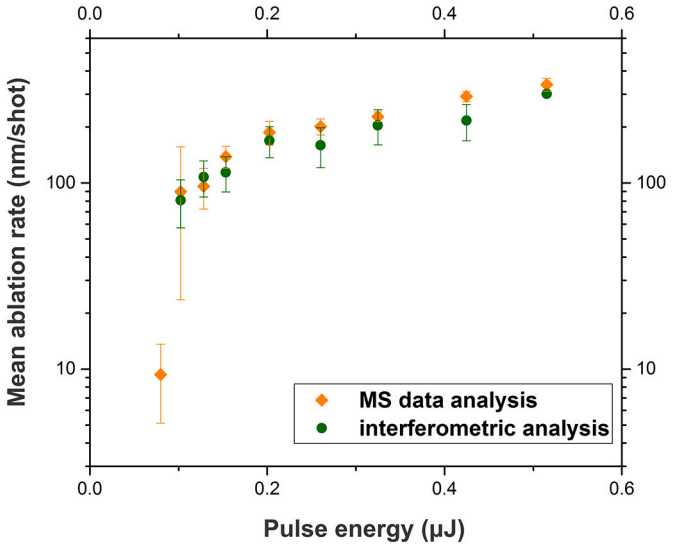

Fig. 8. Mean ablation rate determined by means of mass spectrometric data analysis (orange diamonds) and white light interferometry (green circles) of laser ablation craters obtained with the 258 nm UV fs laser. The mass spectrometric data points were obtained by averaging 5 individual craters generated by 10′000 single laser shots each at different laser pulse energies. The mean ablation rate was calculated based on the onset of the Si signal in the mass spectra. The interferometric data points are derived from craters obtained after application of 500 single laser shots at different laser pulse energies. 3 individual craters were analysed by 2 perpendicular line scans and averaged for each point. Data points are only shown for SnAg-derived ($\leq$ 10 µm) deep craters which could be distinguished from the RMS surface roughness. The lowest shown data point does not represent the ablation threshold. The error bars represent the associated standard deviation of the conducted measurements. (For interpretation of the references to colour in this figure legend, the reader is referred to the web version of this article.)

investigated sample causes noticeable large standard deviations, most pronounced in case of low laser pulse energies, where the crater depth approaches the RMS surface roughness. No interferometrically determined data point is shown for the lowest and highest investigated pulse energies, as the corresponding craters could not be distinguished from the inherent sample surface roughness or might have entered the Si substrate, respectively. The lowest shown data point does not correspond to the ablation threshold.

From PDMS imprints of ideally flat surface samples, the mean ablation rate has previously been determined by measuring the heights of the crater replicas from SEM images of the tilted sample [26]. Yet, because of the substantial surface roughness of the as-deposited SnAg sample, it is very difficult to define a valid reference plane in the SEM images of the PDMS imprints. Nevertheless, the reference plane is a necessary prerequisite for proper height determination via this approach. Therefore, for shallow craters on high surface roughness materials, the mean ablation rate should rather be determined by means of mass spectrometry or white light interferometry on the craters themselves. The latter approaches are significantly less time consuming and more accurate for this purpose. However, PDMS imprints can still contribute valuable information for improved understanding of the ablation process on SnAg alloy. As an example, SEM micrographs of the PDMS imprints (like in Fig. 6), provide the detailed geometry of the conical shape development of the crater with increasing ablation depth, complementing the interferometry line scans. Therefore, a necessary prerequisite for quantitative chemical depth profiling is to account for the change of ablation rate with crater depth, which is a function of the applied pulse energy and the number of applied laser shots. To investigate the dependence of ablation rate on the crater depth, we conducted a parametric study for different pulse energies, comprising craters ranging from 10′000 to only 1 single laser shots each. The analysis of the related craters by means of interferometry is shown in Fig. 9. Note that due to the inherent surface roughness of the sample, data are only available for craters with a depth exceeding the RMS surface roughness which was only the case after a minimum of 50 applied laser shots within the range of tested pulse energies. The upper available data limit is given by the nominal SnAg layer thickness of 10 $\pm$ 2 µm until reaching the Si substrate. The observation of a plateau for large numbers of applied single laser shots at a laser pulse energy of 0.20 µJ is because in this case the laser irradiance is below the ablation threshold of Si. The slope of the trend lines for the individual campaigns drops down with decreasing laser pulse energy, i.e. the effect of increased crater depth on the ablation rate is more pronounced the lower the applied laser pulse energy. This observation needs to be accounted for accurately when interpreting depth profiling results obtained at a given set of experimental settings, which will be addressed in detail in a forthcoming study.

In summary, we find that for fs LIMS analysis of SnAg solder alloy using our LIMS instrument an UV laser with 258 nm wavelength operated at 1 kHz laser pulse repetition rate in an irradiance range above 1 TW/cm^2 allows for locally confined ablation (crater diameter is approximately 10 µm, depending on pulse energy and number of applied single laser shots) independent of the SnAg grain boundaries and without significant thermal effects disturbing the mass spectrometric analysis. Due to the inherent surface roughness and the small crater size, a minimum number of around 50 single laser shots is required to obtain an unambiguously determinable crater at the tested pulse energies. As the sample structures of interest have a limited nominal height of only several tens of µm, it is advisable to operate at pulse energies of about 0.2 µJ to achieve a compromise between an acceptable depth resolution on the one hand and a suitable ablation rate on the other hand to probe the entire sample array down to the Si substrate. The obtained ablation results can be characterized by means of SEM and interferometry to obtain both detailed structural and depth/height information.

4. Conclusions

In this work, we demonstrate how the change from our NIR fs LIMS setup to a UV fs LIMS setup largely expands analysis possibilities for technologically relevant samples, i.e. low melting point, soft, high

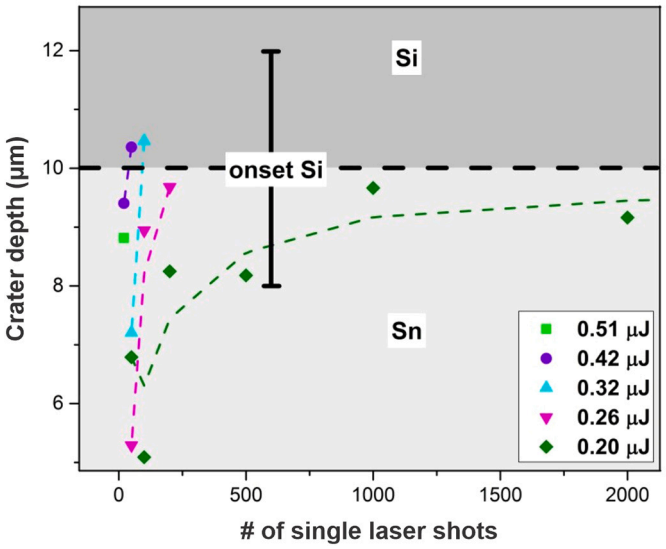

Fig. 9. Crater depth determined by white light interferometry as a function of the number of single UV fs laser shots applied at different laser pulse energies. The slope of the trend lines drops down with decreasing energy and increasing number of applied laser pulses. Only SnAg-derived data are shown in this analysis to assure comparability.

surface roughness, solder alloy samples. We particularly investigate and compare the effects of NIR and UV fs laser ablation for LIMS analysis using our LIMS instrument [23–25] on SnAg solder alloy, which is widely used in the semiconductor industry. SnAg alloy embodies all above mentioned challenging material properties. For the first time we demonstrated herein that for the purpose of spatially resolved chemical analysis of this type of materials, an UV fs laser offers, by far, superior ablation conditions than a NIR fs laser. The advantages of using an UV irradiation source are the significantly reduced thermal effects on the sample, yielding higher ablation rates at similar irradiances, narrower ablation craters, and much better shot-to-shot stability of the ablation process. This is most noticeable at lower laser pulse energies. We are the first to demonstrate that, despite the high surface roughness and the granular structure of the material, it is possible to obtain PDMS imprints of the craters produced in the low melting point SnAg alloy without damaging the sample. Our study proves that interferometric analysis of these imprints provides important complementary information to direct interferometric analysis of the craters as it helps to overcome aspect ratio related difficulties. Despite the sample's roughness, we demonstrate that white light interferometry offers a fast and robust way of obtaining depth/height data on the craters formed in the SnAg sample as well as on their PDMS replicas.

The presented data show that also for rough, low-melting, granularly structured materials as the studied SnAg solder alloy the ablation rate is a function of pulse energy and ablation depth. The first direct comparison of the dependence of this function on the used laser wavelength in fs LIMS studies on a low melting point, high surface roughness material is given herein.

Concerning experimental approaches, we showed that determination of the mean ablation rate for high-surface roughness materials is much faster and more accurate when performed by means of mass spectrometric data analysis or white light interferometry of the laser ablation craters than compared to the SEM-based analysis of the laser ablation craters' PDMS imprints.

Overall, this study contributes to a deepened understanding of ablation processes and the development of ablation rate with crater depth on low melting point, high surface roughness materials which will be used to approach three-dimensional depth profiling of SnAg solder bumps in a forthcoming study.

Declaration of Competing Interest

There are no conflicts to declare.

Acknowledgements

This work was supported by the Swiss National Science Foundation. We gratefully acknowledge the supply of chemicals by BASF SE, Ludwigshafen, Germany and the wafer supply by imec, Leuven, Belgium as well as the technical and material support by IBM Research Zurich, Switzerland. AR acknowledges the support from the European Union's Horizon 2020 research and innovation program under the Marie Skłodowska-Curie grant agreement No. 750353.

Appendix A. Supplementary data

Supplementary data to this article can be found online at https://doi.org/10.1016/j.sab.2021.106145.

References

[1] M. Abtew, G. Selvaduray, Lead-free solders in microelectronics, Mater. Sci. Eng. R. Rep. 27 (2000) 95–141.
[2] J. Woertink, Y. Qin, J. Prange, P. Lopez-Montesinos, I. Lee, Y. Lee, M. Imanari, J. Dong, J. Calvert, From C4 to micro-bump: Adapting lead free solder electroplating processes to next-gen advanced packaging applications, in: 2014 IEEE 64th Electronic Components and Technology Conference (ECTC), 2014, pp. 342–347.
[3] S.-Y. Jang, M.J. Wolf, O. Ehrmann, H. Gloor, H. Reichl, K.-W. Paik, Pb-free Sn/3.5Ag Electroplating Bumping Process and Under Bump Metallization (UBM), Electronics Packaging Manufacturing, IEEE Transactions on 25, 2002, pp. 193–202.
[4] R. Asgari, Semiconductor backend flip chip processing, inspection requirements and challenges, in: 27th Annual IEEE/SEMI International Electronics Manufacturing Technology Symposium, 2002, pp. 18–22.
[5] H. Ezawa, M. Miyata, S. Honma, H. Inoue, T. Tokuoka, J. Yoshioka, M. Tsujimura, Eutectic Sn-Ag solder bump process for ULSI flip chip technology, IEEE Trans. Electron. Packag. Manuf. 24 (2001) 275–281.
[6] J.Y. Kim, J. Yu, J.H. Lee, T.Y. Lee, The effects of electroplating parameters on the composition and morphology of Sn-Ag solder, J. Electron. Mater. 33 (2004) 1459–1464.
[7] V. Venkatasamy, S. Riemer, I. Tabakovic, Electrodeposition of eutectic Sn96.5Ag3.5 films from iodide–pyrophosphate solution, Electrochim. Acta 56 (2011) 4834–4840.
[8] R.E. Galindo, R. Gago, D. Duday, C. Palacio, Towards nanometric resolution in multilayer depth profiling: a comparative study of RBS, SIMS, XPS and GDOES, Anal. Bioanal. Chem. 396 (2010) 2725–2740.
[9] F. Reniers, C. Tewell, New improvements in energy and spatial (x, y, z) resolution in AES and XPS applications, J. Electron Spectrosc. Relat. Phenom. 142 (2005) 1–25.
[10] T.J. Shaffner, Semiconductor characterization and analytical technology, Proc. IEEE 88 (2000) 1416–1437.
[11] E.H. Evans, J. Pisonero, Clare M.M. Smith, R.N. Taylor, Atomic spectrometry update: review of advances in atomic spectrometry and related techniques, J. Anal. At. Spectrom. 33 (2018) 684–705.
[12] D. Käser, L. Hendriks, J. Koch, D. Günther, Depth profile analyses with sub 100-nm depth resolution of a metal thin film by femtosecond - laser ablation - inductively coupled plasma - time-of-flight mass spectrometry, Spectrochim. Acta B At. Spectrosc. 149 (2018) 176–183.
[13] V. Zorba, X. Mao, R.E. Russo, Femtosecond laser induced breakdown spectroscopy of Cu at the micron/sub-micron scale, Spectrochim. Acta B 113 (2015) 37–42.
[14] A. Cedeño López, V. Grimaudo, P. Moreno-García, A. Riedo, M. Tulej, R. Wiesendanger, P. Wurz, P. Broekmann, Towards femtosecond laser ablation ionization mass spectrometric approaches for chemical depth-profiling analysis of lead-free Sn solder bumps with minimized side-wall contributions, J. Anal. At. Spectrom. 33 (2018) 283–293.
[15] V. Grimaudo, P. Moreno-García, A. Cedeño López, A. Riedo, R. Wiesendanger, M. Tulej, C. Gruber, E. Lörtscher, P. Wurz, P. Broekmann, Depth profiling and cross-sectional laser ablation ionization mass spectrometry studies of through-silicon-vias, Anal. Chem. 90 (2018) 5179–5186.
[16] V. Grimaudo, P. Moreno-García, A. Riedo, S. Meyer, M. Tulej, M.B. Neuland, M. Mohos, C. Gütz, S.R. Waldvogel, P. Wurz, P. Broekmann, Toward three-dimensional chemical imaging of ternary Cu–Sn–Pb alloys using femtosecond laser ablation/ionization mass spectrometry, Anal. Chem. 89 (2017) 1632–1641.
[17] P. Moreno-García, V. Grimaudo, A. Riedo, A. Cedeño López, R. Wiesendanger, M. Tulej, C. Gruber, E. Lörtscher, P. Wurz, P. Broekmann, Insights into laser ablation processes of heterogeneous samples: toward analysis of through-silicon-vias, Anal. Chem. 90 (2018) 6666–6674.
[18] C. Geertsen, A. Briand, F. Chartier, J.-L. Lacour, P. Mauchien, S. Sjöström, J.-M. Mermet, Comparison between infrared and ultraviolet laser ablation at atmospheric pressure—implications for solid sampling inductively coupled plasma spectrometry, J. Anal. At. Spectrom. 9 (1994) 17–22.
[19] T.E. Jeffries, W.T. Perkins, N.J.G. Pearce, Comparisons of infrared and ultraviolet laser probe microanalysis inductively coupled plasma mass spectrometry in mineral analysis, Analyst 120 (1995) 1365–1371.
[20] M. Motelica-Heino, O.F.X. Donard, Comparison of UV and IR laser ablation ICP-MS on silicate reference materials and implementation of normalisation factors for quantitative measurements, Geostand. Newslett. 25 (2001) 345–359.
[21] S. Tabatabaei, A. Kumar, H. Ardebili, P.J. Loos, P.M. Ajayan, Synthesis of Au–Sn alloy nanoparticles for lead-free electronics with unique combination of low and high melting temperatures, Microelectron. Reliab. 52 (2012) 2685–2689.
[22] F. Poitrasson, X. Mao, S.S. Mao, R. Freydier, R.E. Russo, Comparison of ultraviolet femtosecond and nanosecond laser ablation inductively coupled plasma mass spectrometry analysis in glass, monazite, and zircon, Anal. Chem. 75 (2003) 6184–6190.
[23] A. Riedo, M. Neuland, S. Meyer, M. Tulej, P. Wurz, Coupling of LMS with a fs-laser ablation ion source: elemental and isotope composition measurements, J. Anal. At. Spectrom. 28 (2013) 1256–1269.
[24] A. Riedo, A. Bieler, M. Neuland, M. Tulej, P. Wurz, Performance evaluation of a miniature laser ablation time-of-flight mass spectrometer designed for in situ investigations in planetary space research, J. Mass Spectrom. 48 (2013) 1–15.
[25] A. Riedo, S. Meyer, B. Heredia, M.B. Neuland, A. Bieler, M. Tulej, I. Leya, M. Iakovleva, K. Mezger, P. Wurz, Highly accurate isotope composition measurements by a miniature laser ablation mass spectrometer designed for in situ investigations on planetary surfaces, Planet. Space Sci. 87 (2013) 1–13.
[26] I.M. Carrasco-García, J.M. Vadillo, J.J. Laserna, Wavelength and energy dependence on ablation dynamics under femtosecond laser pulses observed by time-resolved pump–probe microscopy, Spectrochim. Acta B At. Spectrosc. 158 (2019) 105634.
[27] A. Cedeño López, V. Grimaudo, A. Riedo, M. Tulej, R. Wiesendanger, R. Lukmanov, P. Moreno-García, E. Lörtscher, P. Wurz, P. Broekmann, Three-dimensional

composition analysis of SnAg solder bumps using ultraviolet femtosecond laser ablation ionization mass spectrometry, Anal. Chem. 92 (2020) 1355–1362.
[28] V. Grimaudo, P. Moreno-García, A.C. López, A. Riedo, R. Wiesendanger, M. Tulej, C. Gruber, E. Lörtscher, P. Wurz, P. Broekmann, Combining anisotropic etching and PDMS casting for three-dimensional analysis of laser ablation processes, Anal. Chem. 90 (2018) 2692–2700.
[29] V. Grimaudo, P. Moreno-García, A. Riedo, M.B. Neuland, M. Tulej, P. Broekmann, P. Wurz, High-resolution chemical depth profiling of solid material using a miniature laser ablation/ionization mass spectrometer, Anal. Chem. 87 (2015) 2037–2041.
[30] A. Riedo, M. Tulej, U. Rohner, P. Wurz, High-speed microstrip multi-anode multichannel plate detector system, Rev. Sci. Instrum. 88 (2017), 045114.
[31] S. Meyer, A. Riedo, M.B. Neuland, M. Tulej, P. Wurz, Fully automatic and precise data analysis developed for time-of-flight mass spectrometry, J. Mass Spectrom. 52 (2017) 580–590.
[32] R. Wiesendanger, D. Wacey, M. Tulej, A. Neubeck, M. Ivarsson, V. Grimaudo, P. Moreno-García, A. Cedeño-López, A. Riedo, P. Wurz, Chemical and optical identification of micrometer-sized 1.9 billion-year-old fossils by combining a miniature laser ablation ionization mass spectrometry system with an optical microscope, Astrobiology 18 (2018) 1071–1080.
[33] E. Menard, J. Rogers, Stamping techniques for micro- and nanofabrication, in: B. Bhushan (Ed.), Springer Handbook of Nanotechnology, Springer Berlin Heidelberg, Berlin, Heidelberg, 2007, pp. 279–298.
[34] i.T. Pella. https://www.tedpella.com/Material-Sciences_html/Abrasive_Grit_Grading_Systems.htm, 16.02.2021.
[35] R.E. Russo, Laser ablation, Appl. Spectrosc. 49 (1995) 14A–28A.
[36] S.E. Jackson, H.P. Longerich, G.R. Dunning, B.J. Freyer, The application of laser-ablation microprobe; inductively coupled plasma-mass spectrometry (LAM-ICP-MS) to in situ trace-element determinations in minerals, Can. Mineral. 30 (1992) 1049–1064.
[37] G. Remond, A. Batel, C. Roquescarmes, D. Wehbi, I. Abell, G. Seroussi, Scanning mechanical microscopy of laser ablated volumes related to inductively coupled plasma-mass spectrometry, Scanning Microsc. 4 (1990) 249–274.